

CONTEXTLOSS: CONTEXT INFORMATION FOR TOPOLOGY-PRESERVING SEGMENTATION

Benedict Schacht^{1,2}, Imke Greving², Simone Frintrop¹, Berit Zeller-Plumhoff^{2,3}, Christian Wilms¹

¹University of Hamburg, ²Helmholtz-Zentrum Hereon, ³University of Rostock

ABSTRACT

In image segmentation, preserving the topology of segmented structures like vessels, membranes, or roads is crucial. For instance, topological errors on road networks can significantly impact navigation. Recently proposed solutions are loss functions based on critical pixel masks that consider the whole skeleton of the segmented structures in the critical pixel mask. We propose the novel loss function ContextLoss (CLoss) that improves topological correctness by considering topological errors with their whole context in the critical pixel mask. The additional context improves the network focus on the topological errors. Further, we propose two intuitive metrics to verify improved connectivity due to a closing of missed connections. We benchmark our proposed CLoss on three public datasets (2D & 3D) and our own 3D nano-imaging dataset of bone cement lines. Training with our proposed CLoss increases performance on topology-aware metrics and repairs up to 44 % more missed connections than other state-of-the-art methods. We make the code publicly available^{1, 2}.

Index Terms— Segmentation, Topology-Preserving, Elongated Structures, Loss Function, Bone Cement Line

1. INTRODUCTION

Loss functions are a core component of neural networks, which determine what the network is optimized for. In image segmentation, this translates directly to how well the predictions of the network can resemble the structural properties of the ground truth. The two most commonly used loss functions in image segmentation are the pixel-wise loss functions Dice loss (L_{Dice}) and Cross-Entropy loss (L_{CE}). However, these losses optimize for a maximum overlap of predictions and ground truth by weighting all pixel contributions equally [1, 2]. This is a problem if the topology is of particular interest because the topology is not explicitly considered. This can promote topological errors, eg. in downstream applications related to the segmentation of road systems, blood vessels, or bone features, see Fig. 1.

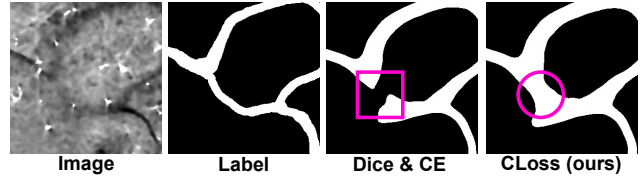


Fig. 1: Motivation. Image segmentation in bone research, where our method improves topological correctness over training with Dice and Cross-Entropy loss (Dice & CE).

Related work [3–8] implements topology sensitivity by applying a pixel-wise loss function (L_{pixel}) like L_{Dice} or L_{CE} on a critical pixel mask of topologically important pixels and combining it with an additional L_{pixel} that is applied on all pixels. Applying L_{pixel} on the critical pixel mask ensures higher network attention on the critical pixels than on the normal pixels. Related work defines the critical pixel mask by including the complete morphological skeletons of ground truth and predictions [3, 4, 8], or a slightly dilated skeleton [5]. [4, 5, 8] extend [3] mainly by different L_{pixel} or removing small structures during training.

While the morphological skeleton is an excellent measure for topological correctness, the complete skeleton typically includes many already correctly predicted pixels. However, the network must be trained to learn a better representation of the topological errors [6, 7]. [6] and [7] identify critical pixel masks at the topological errors without skeletonization at the cost of high runtime. However, their identified critical pixels are either singular pixels [6] or a line of 1-pixel width [7] in the center of the topological errors. Considering only a few singular pixels in the critical pixel mask is a problem because the network can obtain better results if more pixels are included in the mask [9]. We argue that [6] and [7] are missing important context information by including only few critical pixels.

In this paper, we propose the novel loss function CLoss for topology-preserving segmentation. CLoss features an extensive critical pixel mask of the topological errors and particularly considers more context pixels of the topological errors. The additional context pixels are acquired by com-

¹<https://gitlab.com/Benedict.S/ContextLoss>

²Supplement: <https://dx.doi.org/10.60864/jkny-a610>

binning skeletonization and the distance transform. Utilizing skeletonization in the critical pixel selection makes CLoss naturally fast and compatible with 3D data. Our loss can be used on 2D and 3D data with any arbitrary segmentation network to improve topological correctness in a plug-and-play manner. Additionally, we combine our proposed CLoss with a dedicated training strategy to exploit topological post-processing. For validation, we isolate the contribution of our proposed critical pixel mask from the impact of L_{pixel} . We benchmark on four datasets, including our own novel 3D bone Cement Line Dataset (CLD). CLD contains boundary layers of bone tissue which challenge segmentation algorithms with low contrast, diffuse borders, and image artifacts. Further, we propose two intuitive metrics to verify improved connectivity due to a closing of missed connections, which complement existing metrics and are more robust to artifacts from evaluation. In this paper, our contributions can be summarized as follows:

- We propose the novel topology-preserving loss function CLoss which utilizes a critical pixel mask to consider the whole context of topological errors (Sec. 2.1).
- We propose a new 3D bone Cement Line Dataset (CLD) for topology-preserving segmentation (Sec. 3).
- We propose two metrics which are sensitive to missed connections (Sec. 2.2).

2. METHODOLOGY

2.1. ContextLoss

We propose the novel loss function CLoss to promote topology-preserving segmentation with arbitrary segmentation networks. CLoss extracts a critical pixel mask of topologically important locations, which is then considered in the total cost function. In addition, we introduce a pretraining and topological fine-tuning strategy. The results of both stages are combined in a post-processing to generate the final results, see Fig. 2.

Critical pixel mask. The acquisition of the critical pixel mask is illustrated in Fig. 3. The critical pixel mask contains the complete context of all topological errors. We determine the skeleton at the topological critical locations, which is then extended to include all context pixels, using the distance transform. Missed connections are processed as displayed, which we describe below. False positive connections are processed similarly, as mentioned in the caption of Fig. 3.

We first obtain the skeleton of the label. Then, we obtain the skeleton part at the topological error and the correctly predicted skeleton part by splitting the label skeleton to the prediction mask. Then, we apply the distance transform to both splitting results, which calculates the distance of all pixels to the respective split skeleton part. Based on the re-

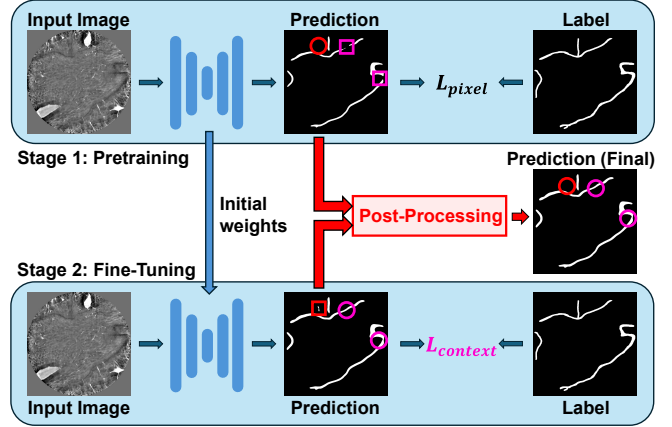


Fig. 2: Our proposed method. An arbitrary segmentation network is pretrained with a standard pixel-wise loss (L_{pixel}) and then fine-tuned with our topology-sensitive CLoss ($L_{context}$). We combine the inference results of the pretraining for topological post-processing with the inference results from the fine-tuning. Our method improves topological correctness (circles) of topological errors (squares).

sults of the distance transforms, the context extraction keeps only the pixels closest to the skeleton split of the topological error (see bottom right in Fig. 3). The context pixel selection is further cropped to label size to focus on the context pixels of the topological error. The resulting critical pixel mask (M) contains all context pixels of missed and false positive connections. See our pseudo-code in the supplement for details (Sec. A.1).

Cost function. Our proposed CLoss is based on a pixel-wise loss function (L_{pixel}), which is adapted for topology-sensitivity. For L_{pixel} , we choose the loss combination of L_{Dice} and L_{CE}

$$L_{pixel} = (1 - \alpha)L_{Dice} + \alpha L_{CE}, \quad (1)$$

with $\alpha \in [0, 1]$ as a weight. For this work, we use $\alpha = 0.5$ for a more robust performance compared to individual L_{Dice} and L_{CE} [1, 10]. We combine L_{pixel} with the critical pixel mask M to our proposed CLoss

$$L_{context} = (1 - \gamma)L_{pixel} + \gamma L_{pixel} \odot M, \quad (2)$$

with the Hadamard product \odot . $\gamma \in [0, 1]$ is a weight to adjust the impact of the topology-sensitive term that contains M .

Training with CLoss. First, a segmentation network is trained with regular L_{pixel} . Subsequently, CLoss is used for fine-tuning to improve topological correctness, see Fig. 2. Empirically, we found a fine-tuning length with 5% of the pretraining length to be most efficient. We include ablations in the supplement (Sec. A.10).

Table 1: Quantitative results. Our dataset, proposed method and proposed metrics are indicated in italic.

Dataset	Method	Weight γ	Dice \uparrow	clDice \uparrow [3]	e \downarrow	e $_1$ \downarrow	e $_0$ \downarrow	e $_0$ -Gt \downarrow	AGS \uparrow
Roads	nnU-Net [10]		79.69	89.34	1.181	0.895	0.286	0.702	86.46
	Dice & CE		79.77	89.37	1.156	0.949	0.207	0.699	86.41
	clDice [3]	0.5	79.50	89.11	1.126	0.897	0.230	0.710	87.07
	Compound clDice	0.3	79.73	89.34	1.108	0.909	0.199	0.673	87.05
	<i>C</i> Loss	<i>0.08</i>	79.82	89.47	1.065	0.880	0.185	0.656	87.70
		<i>0.1</i>	79.57	89.21	0.990	0.810	0.180	0.617	87.88
	<i>0.2</i>	79.12	89.13	0.994	0.788	0.205	0.494	89.48	
HRF-Retina	nnU-Net [10]		82.33	81.88	0.528	0.281	0.247	2.742	77.75
	Dice & CE		82.23	81.69	0.554	0.294	0.260	2.780	77.38
	clDice [3]	0.5	82.15	83.09	0.426	0.256	0.170	2.475	82.23
	Compound clDice	0.5	82.33	82.98	0.405	0.250	0.155	2.429	81.25
	<i>C</i> Loss	<i>0.08</i>	82.22	83.20	0.447	0.259	0.187	2.347	82.28
		<i>0.1</i>	82.20	83.27	0.449	0.262	0.188	2.469	82.61
	<i>0.2</i>	80.57	85.06	0.397	0.225	0.172	1.378	90.39	
Vessap	nnU-Net [10]		92.89	95.83	28.95	1.413	27.54	14.28	96.03
	Dice & CE		93.13	95.81	26.67	1.280	25.39	13.15	96.26
	clDice [3]	0.4	92.70	94.86	29.00	1.240	27.76	9.44	97.74
	Compound clDice	0.1	93.11	95.80	26.10	1.200	24.90	11.68	97.00
	<i>C</i> Loss	<i>0.08</i>	92.91	95.01	26.09	1.227	24.86	9.97	97.85
		<i>0.1</i>	92.28	94.57	27.02	1.300	25.72	9.32	98.03
	<i>0.2</i>	91.69	93.13	25.07	1.827	23.24	6.22	99.04	
CLD	nnU-Net [10]		69.67	83.97	3.243	1.085	2.158	2.493	79.19
	Dice & CE		70.27	85.23	3.422	1.075	2.347	2.447	82.02
	clDice [3]	0.5	70.88	86.22	3.374	1.042	2.333	1.825	87.11
	Compound clDice	0.5	70.61	85.45	3.165	1.065	2.099	2.150	82.66
	<i>C</i> Loss	<i>0.08</i>	70.98	86.22	3.158	1.063	2.095	2.061	84.47
		<i>0.1</i>	70.75	86.26	3.109	1.069	2.040	2.040	84.44
		<i>0.2</i>	70.44	86.83	3.020	1.047	1.973	1.899	85.98
	<i>C</i> Loss (Dice)	<i>0.08</i>	69.43	86.40	3.275	0.969	2.306	1.525	90.51

substantial benefit in this research field to improve the understanding of cement lines. 3D nano-imaging³ of cement lines can specifically improve our understanding of cement lines on the nano-scale. Unfortunately, nano-imaging quality is degraded by noise and various imaging artifacts [18]. Moreover, cement lines have low contrast with respect to their surroundings and diffuse borders. Our CLD consists of 17 3D images of shape $1024^2 \times 600$, featuring a voxel size of $(45.6 \text{ nm})^3$. More details on the annotation process and image acquisition are included in the supplement (Sec. A.4). The characteristics of CLD are distinctly different from current 2D topology-benchmark datasets like Roads [19] and HRF-Retina [20], where the foreground class usually has adequate contrast and clear borders. CLD also features a layer/membrane-like foreground structure that is not included in the 3D topology-benchmark dataset Vessap [21], which has a tubular structure.

³Synchrotron radiation-based full-field transmission X-ray nanotomography operated in Zernike phase contrast microscopy mode [17].

4. EXPERIMENTS

Datasets. Following other work on topology-preserving segmentation [3–8, 13], we use the two public 2D datasets, Massachusetts Roads (Roads) [19] and HRF-Retina [20]. Additionally, we evaluate on two 3D datasets, the public Vessap [21] dataset, and our CLD (Sec. 3). More details on the training splits are included in the supplement (Sec. A.5).

Compared Methods. We use the nnU-Net [10, 22], which provides an optimized standard U-Net [23] for all experiments. We compare CLoss against Dice & Cross-Entropy loss (Dice & CE), clDice [3], and compound clDice. We introduce compound clDice, which corresponds to clDice but has the pixel-wise loss (L_{pixel}) from CLoss. We don't compare against [4, 5, 8], which mainly differ from clDice in L_{pixel} , and [6], which has already been outperformed by clDice. More details on the omitted methods and method optimizations are included in the supplement (Sec. A.6).

Evaluation Metrics. We evaluate all methods with the pixel-wise metric Dice score and the topology-aware metrics cDice [3], Betti Number errors (e , e_0 , and e_1), e_0 -Gt (ours) and AGS (ours). More details on the evaluation are included in the supplement (Sec. A.7).

Implementation Details. The same skeletonization method [3] (50 iterations) is used for all corresponding methods. We apply our proposed topological post-processing (Sec. 2.1) to all fine-tuning results to highlight the impact of our proposed loss function. Ablations for our proposed topological post-processing are provided in the supplement (Sec. A.10). We perform five-fold cross-validations for all methods. Further details are included in the supplement (Sec. A.8).

4.1. Results and Discussion

The quantitative results of our experiments are displayed in Tab. 1. Our proposed CLoss achieves the best overall topology performance on all datasets, indicated by the combined betti error e . This is supported by the superior gap closing of CLoss for all datasets, indicated by e_0 -Gt and AGS. For HRF-Retina, CLoss repairs 44% more missed connections than cDice (e_0 -Gt). CLoss achieves the best performance for the cDice metric in all datasets except for Vessap, which can be attributed to skeletonization artifacts connected to the complex surface structure of Vessap in combination with thickened predictions from CLoss, see Fig. 4. CLoss consistently outperforms compound cDice on the topology metrics, which only differs from CLoss in the critical pixel mask, and to cDice only in L_{pixel} . Hence, we conclude a superior critical pixel mask of our CLoss compared to cDice in the scope of our experiments. Losses with L_{Dice} for L_{pixel} have a slight advantage on CLD, so we added CLoss (Dice) for comparison with cDice, which has the same L_{pixel} as cDice. We observe for all datasets, that superior gap closing (better e_0 -Gt and AGS) is linked with a stronger weighting of CLoss, which is intuitively expected. Better overall topological performance (e) and gap closing (e_0 -Gt and AGS) is also linked with a decreased Dice score for all datasets.

Our quantitative results are supported by our qualitative results in Fig. 5, where we compare CLoss ($\gamma = 0.2$) with Dice & CE. The predictions with CLoss have significantly higher topological correctness than those of Dice & CE, highlighted by the green arrows. For HRF-Retina, CLoss repairs especially many missed connections and doesn't introduce visible false positive connections. All predictions of CLoss have a slightly higher thickness than the ground truth and Dice & CE, see Fig. 5. This observed higher thickness confirms that the decreasing Dice score for higher weights of CLoss in Tab. 1 originates mainly from an increased thickness of the predictions and is compensated by increasing topological

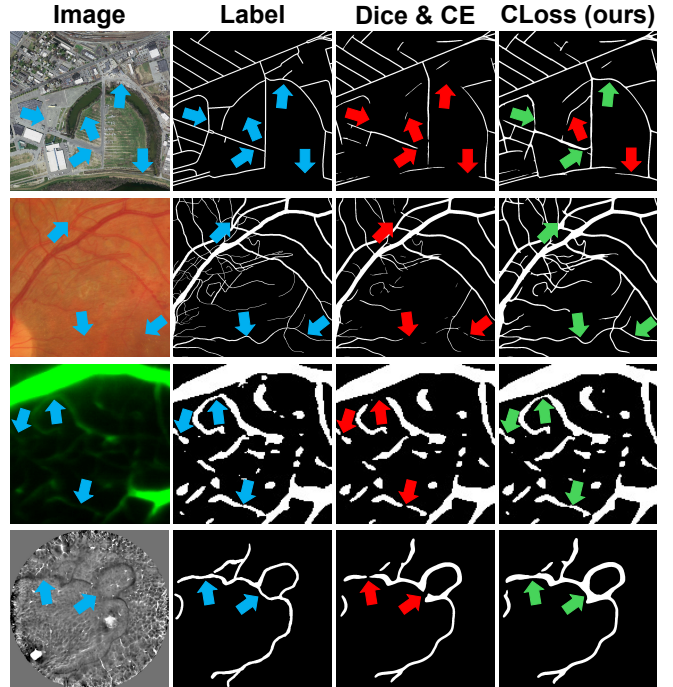


Fig. 5: Qualitative results. The sampled patches are from Roads, HRF-Retina, Vessap, and CLD (up to down). Arrows indicate high (green) and low (red) topological correctness with respect to the input image/label (blue).

correctness. CLoss runtime with soft skeletonization [3] is comparable to cDice, which is orders of magnitude faster than [6, 7, 13], as compared in [13]. We include a more detailed discussion, runtimes and ablation results in the supplement (Sec. A.9, Sec. A.10).

5. CONCLUSION

In this work, we propose the novel topology-preserving loss function CLoss. CLoss is based on a critical pixel mask, which considers the whole context of topological errors. We implement CLoss with a dedicated training strategy that allows for topological post-processing. CLoss can be used on 2D and 3D datasets with any arbitrary segmentation network. Further, we benchmark on our own 3D dataset CLD, which features low contrast, diffuse borders, and image artifacts. Additionally, we propose two intuitive metrics to verify improved connectivity due to a closing of gaps. We demonstrate the superiority of our context-based critical pixel mask over the critical pixel mask of the entire skeletons on all of our four experiment datasets, where CLoss repairs up to 44% more missed connections than other state-of-the-art methods.

Acknowledgement. We acknowledge the support by DASHH (Data Science in Hamburg - HELMHOLTZ Graduate School for the Structure of Matter) with the Grant-No. HIDSS-0002.

6. REFERENCES

- [1] J. Ma, J. Chen, M. Ng, R. Huang, Y. Li, C. Li, X. Yang, and A. L. Martel, "Loss odyssey in medical image segmentation," *MedIA*, vol. 71, 2021.
- [2] B. Liu, J. Dolz, A. Galdran, R. Kobbi, and I. Ben Ayed, "Do we really need dice? the hidden region-size biases of segmentation losses," *MedIA*, vol. 91, 2024.
- [3] S. Shit, J. C. Paetzold, A. Sekuboyina, I. Ezhov, A. Unger, A. Zhylyka, J. W. Pluim, U. Bauer, and B. H. Menze, "cDice - a Novel Topology-Preserving Loss Function for Tubular Structure Segmentation," in *CVPR*, 2021.
- [4] M. J. Menten, J. C. Paetzold, V. A. Zimmer, S. Shit, I. Ezhov, R. Holland, M. Probst, J. A. Schnabel, and D. Rueckert, "A skeletonization algorithm for gradient-based optimization," in *ICCV*, 2023.
- [5] Y. Kirchhoff, M. R. Rokuss, S. Roy, B. Kovacs, C. Ulrich, T. Wald, M. Zenk, P. Vollmuth, J. Kleesiek, F. Isensee, and K. Maier-Hein, "Skeleton recall loss for connectivity conserving and resource efficient segmentation of thin tubular structures," in *ECCV*, 2024.
- [6] X. Hu, F. Li, D. Samaras, and C. Chen, "Topology-preserving deep image segmentation," *NeurIPS*, vol. 32, 2019.
- [7] X. Hu, "Structure-aware image segmentation with homotopy warping," in *NeurIPS*, 2022, vol. 35.
- [8] C. Acebes, A. H. Moustafa, O. Camara, and A. Galdran, "The centerline-cross entropy loss for vessel-like structure segmentation: Better topology consistency without sacrificing accuracy," in *MICCAI*, 2024.
- [9] K. Gotkowski, C. Lüth, P. F. Jäger, S. Ziegler, L. Krämer, S. Denner, S. Xiao, N. Disch, K. H. Maier-Hein, and F. Isensee, "Embarrassingly simple scribble supervision for 3d medical segmentation," *arXiv preprint arXiv:2403.12834*, 2024.
- [10] F. Isensee, P. F. Jaeger, S. A. A. Kohl, J. Petersen, and K. H. Maier-Hein, "nnU-Net: a self-configuring method for deep learning-based biomedical image segmentation," *Nature Methods*, vol. 18, no. 2, 2021.
- [11] L. Maier-Hein and et al., "Metrics reloaded: recommendations for image analysis validation," *Nature Methods*, vol. 21, no. 2, 2024.
- [12] Alexander H. Berger, Laurin Lux, Alexander Weers, Martin Menten, Daniel Rueckert, and Johannes C. Paetzold, "Pitfalls of topology-aware image segmentation," *arXiv preprint arXiv:2412.14619*, 2024.
- [13] L. Lux, A. H. Berger, A. Weers, N. Stucki, D. Rueckert, U. Bauer, and J. C. Paetzold, "Topograph: An efficient graph-based framework for strictly topology preserving image segmentation," in *ICLR*, 2025.
- [14] L. Li, Q. Ma, C. Ouyang, Z. Li, Q. Meng, W. Zhang, M. Qiao, V. Kyriakopoulou, J. V. Hajnal, D. Rueckert, and B. Kainz, "Robust segmentation via topology violation detection and feature synthesis," in *MICCAI*, 2023.
- [15] B. A. Lamarche, J. S. Thomsen, C. M. Andreasen, T. L. Andersen, and W. B. Lievers, "Trabecular bone structural units and their cement lines change with age, bone volume fraction, structure, and strength in female human vertebrae," *JBMR Plus*, vol. 9, no. 1, 2024.
- [16] T. A. Grünewald, A. Johannes, N. K. Wittig, J. Palle, A. Rack, M. Burghammer, and H. Birkedal, "Bone mineral properties and 3D orientation of human lamellar bone around cement lines and the Haversian system," *IUCrJ*, vol. 10, no. 2, 2023.
- [17] E. Longo, L. Sancey, S. Flenner, A. Kubec, A. Bonnin, C. David, M. Müller, and I. Greving, "X-ray Zernike phase contrast tomography: 3D ROI visualization of mm-sized mice organ tissues down to sub-cellular components," *Biomed. Opt. Express*, vol. 11, no. 10, 2020.
- [18] S. Sefa, J. Espiritu, H. Ćwieka, I. Greving, S. Flenner, O. Will, S. Beuer, D.C F. Wieland, R. Willumeit-Römer, and B. Zeller-Plumhoff, "Multiscale morphological analysis of bone microarchitecture around mg-10gd implants," *Bioactive Materials*, vol. 30, 2023.
- [19] Volodymyr Mnih, *Machine Learning for Aerial Image Labeling*, Ph.D. thesis, University of Toronto, 2013.
- [20] A. Budai, R. Bock, A. Maier, J. Hornegger, and G. Michelson, "Robust Vessel Segmentation in Fundus Images," *International Journal of Biomedical Imaging*, vol. 2013, no. 1, 1 2013.
- [21] M. I. Todorov, J. C. Paetzold, O. Schoppe, G. Tetteh, V. Efremov, K. Völgyi, M. Düring, M. Dichgans, M. Piraud, B. Menze, and A. Ertürk, "Automated analysis of whole brain vasculature using machine learning," *bioRxiv*, 2019.
- [22] F. Isensee, T. Wald, C. Ulrich, M. Baumgartner, S. Roy, K. Maier-Hein, and P. F. Jäger, "nnU-Net Revisited: A Call for Rigorous Validation in 3D Medical Image Segmentation," in *MICCAI*, 2024.
- [23] O. Ronneberger, P. Fischer, and T. Brox, "U-net: Convolutional networks for biomedical image segmentation," in *MICCAI*, 2015.

in theory be achieved with a post-processing of opening and erosion operations. However, the applicability of opening and erosion operations depends highly on the predicted structures. Opening and erosion operations have a high risk of introducing new false positive connections that weren't present before the post-processing. Our suggested post-processing is by design robust to introducing new artifacts in the form of false positive connections.

Compared to the runtime solution of [5], our approach doesn't require any additional hyperparameters to select the size of the removed structures and will also remove artifacts which are missed by a fixed threshold.

A.4. Cement line dataset (CLD)

Image Acquisition. Specific steps for acquiring the used 3D images of the nanotomography bone cement line dataset are described in [18], sections 2.4.2 to 2.4.4.1. These steps include the preparation of the imaged specimen, the imaging procedure and the processing of the raw images. We cropped the images from their initial shape $1024^2 \times 1024$ to their final shape $1024^2 \times 600$ to focus on areas with pronounced cement lines and minimal artifacts.

Annotation. The annotation was done for each image on the complete initial shape of $1024^2 \times 1024$. The annotation of the cement lines was done manually in Avizo (version 2024.2, Thermo Fisher Scientific, Waltham, USA), utilizing the standard brush and interpolation tools. The cement lines have low contrast and diffuse borders. Importantly, their visibility and area proportion in the 2D view of the 3D image critically depends on the view angle in 3D, which doesn't always align well with the available view axes (xy, xz, zy). When the cement lines slightly change orientation inside the bone they can become much less pronounced in the current 2D view direction and significantly change in the displayed size.

To address these issues, we conducted a pre-annotation for all 3D images from all three view angles (axes: xy, xz, zy) to acquire a coarse initial representation of all cement lines. The pre-annotation corresponds to a detailed annotation about every 50 slices for each view axis for every 3D image. The pre-annotation was used to determine the preferred orientation of the majority of the cement lines within the 3D image. The pre-annotation was further used as an aid in the more thorough annotation to not miss any cement lines due to viewing angle effects. The thorough annotation was done along the most suitable view axis (xy, xz , or zy). This most suitable view axis was chosen in a way that the majority of the cement lines had a small area proportion in the 2D view of the 3D image, see Fig. 7. The thorough annotation corresponds to a detailed annotation about every three to five slices along

the most suitable view axis for every 3D image. The thorough annotation for each 3D image was then interpolated with the standard Avizo interpolation tool. This interpolation was designed by Avizo to only interpolate between annotation slices without considering any gray values. However, the resulting annotation was a suitable compromise between annotation time and annotation accuracy.

Sometimes, the interpolation tool didn't work as expected, and there were holes within the annotation that didn't get interpolated. To close these interpolation holes, we conducted a series of morphological opening and closing operations until the holes were closed. We repeated this step with additional annotated slices when this approach didn't work initially. We note that the interpolation had also severe trouble interpolating more than one cement line at a time. As a solution, we conducted the thorough annotation and interpolation procedure only for selected parts of a single cement line at once, which we later combined into the complete annotation.

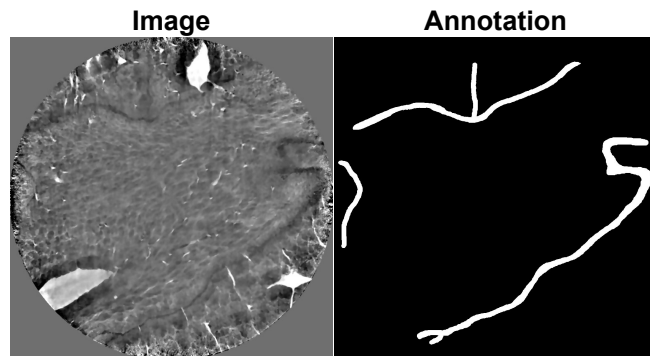


Fig. 7: Cement line Annotation. The cement lines have low contrast and diffuse borders. Also, their appearance is diffuse, note in the left image the changing grayscale characteristics of the cement line in the lower right corner from bottom to right.

A.5. Datasets

Roads contains aerial images (1500^2) of the road system in Massachusetts, similar to settings in [3] and [7] we use 421 images for training and 49 for testing, after excluding images with a white-masked pixel percentage of more than 4%. HRF-Retina consists of high-resolution fundus images (3504×2336) for retinal vessel segmentation, we use 36 images for training and 9 for testing. Vessap contains volumetric scans ($500^2 \times 50$) of brain vessels in two channels, similar to settings in [3] we use 8 3D images for training and 3 for testing, using both input channels simultaneously. Our CLD contains volumetric scans ($1024^2 \times 600$) of bone cement lines, we use 13 3D images for training and 4 for testing. We conduct a five-fold cross-validation for all datasets.

We further note that the high-resolution of HRF-Retina is especially suited for examining the influence of the critical pixel mask as the topological errors are represented by more pixels than in lower-resolution images.

A.6. Compared Methods

The nnU-Net [10] is a framework that provides an improved version of the standard U-Net [23] with optimized hyperparameters. The nnU-Net is by default trained with a compound loss, consisting of Dice and Cross-Entropy loss [1].

clDice [3] is another topology-aware segmentation loss based on critical pixels that focuses on the extracted skeleton of likelihood maps and ground truth masks.

Method optimization. To demonstrate the effectiveness and better topological performances of our proposed method, we ensure identical prerequisites of our proposed method and the compared methods so that better performance can be clearly attributed to our proposed critical pixel mask. In that spirit, we conduct hyperparameter optimizations not only for our proposed method but also for the compared methods. For compound clDice, we conducted a weight hyperparameter search for each dataset ranging from 0.1 to 0.5 in 0.1 steps. For space reasons, we only report the compound clDice result with the highest clDice metric in Tab. 1. For clDice, we use the weight with the highest clDice metric for each dataset from their paper. For CLD, we choose the same weight for clDice as for the optimized compound clDice.

Omitted Methods. We compare against clDice loss [3], a state-of-the-art topology-aware segmentation loss, which defines the skeleton of predictions and ground truth as critical pixel mask. clDice and [8] only differ in L_{pixel} . clDice and [4] only differ in the skeleton algorithm, having the same L_{pixel} and critical pixel mask. [5] is the multi-class adaption of clDice with a different L_{pixel} and a reduced critical pixel mask in comparison to clDice that only includes the slightly dilated ground truth skeleton for computational efficiency. Additionally, [5] removes small structures during training which makes it difficult to point out from which design-choice their reported improvement over clDice (no removed structures) originates. However, as [5] note themselves an inferior skeleton extraction for binary segmentation compared to clDice, we suspect their critical pixel mask selection to be inferior to clDice in binary segmentation as it doesn't consider false positive connections.

Our proposed method can be adapted with any skeleton extraction and L_{pixel} . Hence, we focus on validation against methods with a distinctly different critical pixel mask selection strategy. Therefore, we don't validate against [4, 8] and [5], which use different skeletonization methods or L_{pixel}

than clDice but not superior critical pixel masks. CLoss outperforming compound clDice implies CLoss outperforming [4, 5, 8].

We would have liked to compare against [7] but weren't able to reproduce their results. We could only reproduce their proposed critical pixel mask for the 2D datasets but not on our 3D CLD. We suspect that this might be caused by the complex 3D surface structure in our CLD. Initial training attempts with the original code from their repository resulted in numerous errors for the 2D and 3D datasets, which we could only fix for the 3D datasets. However, related work [5, 8, 13, 14] also doesn't report results on [7], so the implementation of [7] might be a common issue.

There also exist numerous other topology-preserving approaches that we don't compare against, since this would go well beyond the scope of this paper. These other approaches are not based on critical pixel masks and include for example graph-based approaches [13] ([13] only works with 2D data) or approaches entirely based on post-processing [14] (omits to improve topology correctness already in the image domain). We note that [14] can be complemented with our proposed method.

A.7. Evaluation Metrics

Evaluation patch sizes. We evaluated the Dice metric respectively over the whole test samples for the used 2D and 3D datasets.

As mentioned in Sec. 2.2, e_0 is not able to capture gaps if it is computed over the whole image for datasets with high overall connectivity. We calculate the metrics on patch sizes which provide meaningful evaluation for the used datasets. We iterate over the whole image shape with the patches as sliding window (similar to [8]) instead of sampling patches randomly for evaluation like [3, 6, 7, 13].

For 2D datasets, we evaluate clDice and AGS on the whole image. We calculate betti-metrics and e_0 -Gt on patches, 375^2 (Roads) and 292^2 (HRF-Retina).

For the 3D dataset Vessap, we calculate clDice, AGS and e_0 -Gt over the whole sample volume. We calculate betti-metrics on full image size along the z-direction.

For our 3D CLD, we calculate clDice, AGS and e_0 -Gt over patches of $1024^2 \times 64$, where we also consider corrections of the clDice metric for its shortcoming with empty patches. We note that this patching in comparison to Vessap is due to memory reasons. Further, we evaluate betti-metrics on full image size along the z-direction.

A.8. Implementation Details

We conduct all our trainings within the nnU-Net framework [10] to ensure a maximum of reproducibility and leading performance [22]. The nnU-Net standard training has a length of 1000 epochs and utilizes Dice and Cross-Entropy as equally weighted compound loss. Training is done with a five-fold cross-validation for all methods. Inference is by standard done with all five folds simultaneously as an ensemble.

For our 2D datasets, we use the nnU-Net configuration 2d. For our 3D datasets, we use the configuration 3d_fullres.

We used the standard nnU-Net configuration for all methods, meaning our results can be reproduced with any GPU that has more than 11 GB VRAM. For increased speed, we conduct all trainings on A100 GPUs. As our used datasets are comparably small, we use the standard nnU-Net configuration without the residual encoder presets. We use PyTorch framework version 2.3.0 to implement our proposed method.

The nnU-Net configured a batch size of two for all datasets. The patch sizes for the 2D datasets were configured by nnU-Net to 1280×1024 (Roads), 1536×1024 (HRF-Retina) and for the 3D datasets to $256^2 \times 32$ (Vessap) and $160^2 \times 90$ (CLD).

For connectivity, we apply 8-adjacency in 2D and 26-adjacency in 3D.

Inference. Alg. 2 displays the pseudo-code for the inference with our proposed training-regime from Fig. 2.

Algorithm 2 CLoss inference

Input: D	% domain image
$X_{bin}^{pre} \leftarrow predictions_{Pretraining}(D)$	% Binarized
$X_{bin}^{ft} \leftarrow predictions_{fine-tuning}(D)$	% Binarized
$X_{bin} \leftarrow post-processing(X_{bin}^{pre}, X_{bin}^{ft})$	% Only keeps structures of X_{bin}^{ft} already present in X_{bin}^{pre}
Output: X_{bin}	% Binarized final predictions

Guideline for tuning gamma. If γ tends to 0, CLoss will converge to Dice&CE loss. A higher γ encourages more topological correctness. It should be $\gamma < 0.5$ to not focus overly on topological errors. All our datasets show good results for a value of 0.2. For new datasets, we recommend the common exploration approach in multiples of 3, e.g. 0.3, 0.1, 0.03.

Comment on generalization of CLoss to object segmentation of tumours and organs. CLoss promotes topology-preserving segmentation along the skeleton-pixels of the predictions and ground truth. Therefore, CLoss can be beneficial in all areas where the skeleton-pixels yield desirable information. We note that skeleton-pixels are typically not important for spherical objects like the human heart but are of increased importance for elongated objects like the trachea.

A.9. Additional Discussion of Quantitative Results

HRF-Retina. CLoss has the smallest error on the number of connected components (e_0) in all datasets except for HRF-Retina. We attribute the value for HRF-Retina to the mentioned susceptibility of e_0 to artifacts (Sec. 2.2) from the patch-based evaluation. The artifact distortion of e_0 is indicated by e_0 -Gt, AGS, and the cIDice metric. Our proposed metrics e_0 -Gt and AGS clearly show a better gap closing of CLoss. Additionally, also the cIDice metric of CLoss for HRF-Retina is significantly improved (about 2%) over its closest competing method. The cIDice metric is especially reliable for HRF-Retina due to the smooth surface structure of the vessels. This indicates a better topology performance of CLoss for HRF-Retina despite the seemingly unfavorable e_0 value.

Vessap. For the Vessap dataset, we observe that the best cIDice score is achieved by the topology-insensitive nnU-Net (pretraining). This seems to contradict with the other topology-sensitive metrics. Therefore, we suspect that the thin network 3D structures of Vessap could lead to many seemingly false positive predictions of the prediction skeleton, which distorts the topological sensitivity of the cIDice metric on this dataset, see Fig. 4. This hypothesis is supported by an increasing AGS score for the topological fine-tuned methods. We also note that the seemingly high e_0 values for Vessap come from our patch-based evaluation of (full 2D image sizes stepping along the z-direction) in combination with the 3D network structure of Vessap. We note that e_1 in this context can especially contain artifacts from the slicing. Therefore, a minimized e_0 indicates topological performance on Vessap more reliable than minimized e_1 .

CLD. The unmodified cIDice loss only has a better gap closing (better e_0 -Gt and AGS) than our standard CLoss on CLD. Importantly, this is only due to a different pixel-wise loss and not due to the different critical pixel mask. We verify this by adding results of CLoss (Dice) to CLD, which has the same pixel-wise loss function as cIDice and only differs in the critical pixel mask to the cIDice loss. CLoss (Dice) visibly outperforms cIDice on the topology metrics. Interestingly, CLoss (Dice) is better than our proposed standard CLoss in e_1 , e_0 -Gt, and AGS but not in cIDice, e , and e_0 . This indicates that the target structure of our CLD favors different L_{pixel} for

different metrics, which is not the case for the other datasets (compound cIDice consistently better or comparable to original cIDice). The favoring of different L_{pixel} for different metrics further illustrates the increased complexity of CLD over the other datasets.

Generating predictions on the test set is independent of the utilized loss and takes about 3min for the Roads dataset.

A.10. Ablations

Post-Processing. Additional results of the post-processing are displayed in Tab. 2. All metric values in this example improve except for e_1 , which remains the same, and AGS, which slightly decreases. All methods benefit from our post-processing in a similar quantity. It can be observed for all results, that the change in the Dice value is comparably small to the change in e . This indicates, that our post-processing primarily removes noise in the form of small separated structures.

Fine-tuning length. Ablations for the fine-tuning length are displayed in Tab. 3. A shorter fine-tuning length seems preferable, although we note that there is no consistent trend between the different lengths. For more detailed ablations on the fine-tuning between 50 epochs and 100 epochs, there was no clear winner, as might be falsely suggested by Tab. 3. Hence, we chose 50 epochs for computational efficiency.

Critical pixel mask. Additional ablations for the critical pixel mask are included in Tab. 4. We include Thin CLoss, which has a critical pixel extraction analog to CLoss except for the context extraction. Therefore, Thin CLoss only considers the skeleton at the topological errors. Our proposed critical pixel mask with context extraction yields significantly better topological correctness. CLoss seems only second best in e_1 to compound cIDice ($\gamma = 0.1$), but the other bad metric values of compound cIDice ($\gamma = 0.1$) indicate that this is likely not due to overall topological correctness but rather related to artifacts.

Pixel-wise loss. An ablation on L_{pixel} is included in Tab. 5. cIDice and compound cIDice differ only in L_{pixel} . cIDice has L_{Dice} , and compound cIDice the equally weighted combination of L_{Dice} and L_{CE} , analogue to our CLoss implementation. Compound cIDice performs better on average for Roads, HRF-Retina, and Vessap. For CLD we note an advantage for cIDice.

Compound cIDice optimization. Additional results of the compound cIDice optimization are displayed in Tab. 6. CLoss yields consistently better results.

Runtime. Results on the runtime are displayed in Tab. 7. The runtime of CLoss is comparable to cIDice. In perspective, other state-of-the-art approaches [6, 7, 13] have 10 to 60 times longer loss calculations than cIDice, as compared by [13].

Table 2: Post-Processing. Example for CLD.

Post-Processing	Method	Weight γ	Dice \uparrow	cIDice \uparrow [3]	e \downarrow	e $_1\downarrow$	e $_0\downarrow$	e $_0-Gt\downarrow$	AGS \uparrow
w/o	Dice & CE		70.23	85.17	3.615	1.075	2.540	2.479	82.03
with			70.27	85.23	3.422	1.075	2.347	2.447	82.02
w/o	Compound cIDice	0.5	70.58	85.39	3.325	1.065	2.259	2.176	82.67
with			70.61	85.45	3.165	1.065	2.099	2.150	82.66
w/o	<i>C</i> Loss	0.2	70.41	86.75	3.224	1.047	2.177	1.916	85.99
with			70.44	86.83	3.020	1.047	1.973	1.899	85.98

Table 3: Fine-tuning length. Example for CLD. All results are post-processed.

Epochs	Method	Weight γ	Dice \uparrow	cIDice \uparrow [3]	e \downarrow	e $_1\downarrow$	e $_0\downarrow$	e $_0-Gt\downarrow$	AGS \uparrow
50	Compound cIDice	0.5	70.61	85.45	3.165	1.065	2.099	2.150	82.66
100			70.67	85.37	3.108	1.062	2.046	2.086	82.79
150			70.58	85.22	3.097	1.064	2.034	2.180	82.19
300			70.65	85.44	3.115	1.053	2.062	2.097	82.71
50	<i>C</i> Loss	0.1	70.75	86.26	3.109	1.069	2.040	2.040	84.44
100			70.77	86.25	3.046	1.050	1.996	2.010	84.78
150			70.46	85.64	3.173	1.062	2.110	2.218	83.02
300			70.51	85.34	3.075	1.060	2.015	2.079	82.39

Table 4: Critical pixel mask. Example for CLD. All results are post-processed. All methods differ only in the critical pixel mask.

Critical pixel mask	Method	Weight γ	Dice \uparrow	cIDice \uparrow [3]	e \downarrow	e $_1\downarrow$	e $_0\downarrow$	e $_0-Gt\downarrow$	AGS \uparrow
w/o	Dice & CE		70.27	85.23	3.422	1.075	2.347	2.447	82.02
Full skeleton	Compound cIDice	0.1	68.93	83.11	3.522	1.029	2.493	2.679	79.06
		0.2	70.47	84.96	3.361	1.077	2.283	2.352	81.81
		0.3	70.61	85.41	3.230	1.077	2.153	2.249	82.80
		0.4	70.51	85.16	3.287	1.063	2.223	2.283	82.26
		0.5	70.61	85.45	3.165	1.065	2.099	2.150	82.66
Skeleton at topological errors	<i>Thin C</i> Loss	0.08	70.33	85.06	3.353	1.087	2.266	2.438	81.53
		0.2	69.76	84.39	3.356	1.095	2.261	2.492	79.66
		0.5	69.62	84.05	3.475	1.091	2.383	2.643	79.29
Context at topological errors	<i>C</i> Loss	0.08	70.98	86.22	3.158	1.063	2.095	2.061	84.47
		0.1	70.75	86.26	3.109	1.069	2.040	2.040	84.44
		0.2	70.44	86.83	3.020	1.047	1.973	1.899	85.98

Table 5: Pixel-wise loss. We focus on ablation between L_{Dice} and our L_{pixel} used for *C*Loss. All results are post-processed.

Dataset	Method	Weight γ	Dice \uparrow	cIDice \uparrow [3]	e \downarrow	e $_1\downarrow$	e $_0\downarrow$	e $_0-Gt\downarrow$	AGS \uparrow
Roads	cIDice [3]	0.5	79.50	89.11	1.126	0.897	0.230	0.710	87.07
	Compound cIDice	0.5	79.59	89.21	1.065	0.870	0.195	0.673	87.25
HRF-Retina	cIDice [3]	0.5	82.15	83.09	0.426	0.256	0.170	2.475	82.23
	Compound cIDice	0.5	82.33	82.98	0.405	0.250	0.155	2.429	81.25
Vessap	cIDice [3]	0.4	92.70	94.86	29.00	1.240	27.76	9.44	97.74
	Compound cIDice	0.4	92.98	95.42	26.880	1.220	25.660	11.040	97.28
<i>CLD</i>	cIDice [3]	0.5	70.88	86.22	3.374	1.042	2.333	1.825	87.11
	Compound cIDice	0.5	70.61	85.45	3.165	1.065	2.099	2.150	82.66

Table 6: Compound cIDice optimization. Example for Roads dataset. All results are post-processed.

Method	Weight γ	Dice \uparrow	cIDice \uparrow [3]	$e\downarrow$	$e_1\downarrow$	$e_0\downarrow$	$e_0-Gt\downarrow$	AGS \uparrow
nnU-Net [10]		79.69	89.34	1.181	0.895	0.286	0.702	86.46
Dice & CE		79.77	89.37	1.156	0.949	0.207	0.699	86.41
Compound cIDice	0.1	79.69	89.26	1.089	0.866	0.223	0.691	86.78
	0.2	79.59	89.12	1.082	0.880	0.202	0.708	86.87
	0.3	79.73	89.34	1.108	0.909	0.199	0.673	87.05
	0.4	79.68	89.26	1.125	0.915	0.210	0.677	87.05
	0.5	79.59	89.21	1.065	0.870	0.195	0.673	87.25
<i>C</i> Loss	0.08	79.82	89.47	1.065	0.880	0.185	0.656	87.70
	0.1	79.57	89.21	0.990	0.810	0.180	0.617	87.88
	0.2	79.12	89.13	0.994	0.788	0.205	0.494	89.48

Table 7: Runtime. Example for Roads dataset.

Loss	Time/epoch	Time/training
Dice & CE	22s	29min
cIDice	63s	59min
<i>C</i> Loss	78s	71min